



Research paper

Improved Terzaghi-theory-based interaction modeling of rotary robotic locomotors with granular substrates



Chuanxiao Yang^a, Liang Ding^{a,*}, Dewei Tang^a, Haibo Gao^a, Lizhou Niu^a, Qingning Lan^a, Chen Li^b, Zongquan Deng^a

^a State Key Laboratory of Robotics and System, Harbin Institute of Technology, Harbin 150001, China

^b Department of Mechanical Engineering, Johns Hopkins University, Baltimore, MD 21218, USA

ARTICLE INFO

Article history:

Received 1 February 2020

Revised 17 March 2020

Accepted 30 March 2020

Available online 21 May 2020

Keywords:

Interaction mechanics

Rotary robot legs

Granular substrates

Terzaghi theory

Terramechanics

ABSTRACT

When legged animals and robots move on granular substrates such as loose sand, their legs may sink below the terrain, rowing and paddling within the granular media. However, conventional leg-ground contact models such as elastic and elastoplastic models are unavailable to describe the rotary interaction of penetrated legs which is affected by the flowability of the particles. Therefore, an improved sliding theory was developed to predict ground reaction forces generated by robotic locomotors that rotate through granular media. The conventional sliding assumptions proposed by Terzaghi were developed to estimate the critical forces exerted on the retaining walls of building foundations, whose lateral size are sufficiently large that they are often assumed to be infinitely wide. An improvement to the width of a robotic leg, affected by both the properties of soil and the dimensions of the leg, was developed in the improved sliding model. The results demonstrate the high fidelity of the improved model in predicting interaction forces at a penetration phase during rotation, without considering the digging motion phase, with a goodness of fit larger than 90%.

© 2020 Elsevier Ltd. All rights reserved.

1. Introduction

The main advantages of legged locomotion are its adaptability and maneuverability on rough terrains [1,2]. For instance, the bio-inspired quadruped robot BigDog was expected to walk on debris and ladders while carrying heavy loads [3]. However, walking on a deformable surface remains a challenge for legged locomotors because of ground deformation and flow. Undesired penetration will be generated if the locomotor load is larger than the resistive force of particles [4], which will reduce the locomotor performance.

For the robot named SandBot with cockroach-inspired leg design studied at the Georgia Institute of Technology [5] (a small RHex-type robot developed in KodLab at University of Pennsylvania [6,7]), the moving speed is highly sensitive to limb frequency and packing fraction, which is defined as the ratio of solid grain volume to occupied volume [4,8]. The robot's C-shaped legs act as a force-generating paddle while penetrating into the terrain composed of particles of low resistive strength [4,9]. Its leg-ground interaction mechanism is similar to that of the desert-dwelling zebra-tailed lizard [4,5], whose paws can intrude into substrates instead of stepping on surfaces as camels do (as illustrated in Fig. 1). The C-shaped legs of the RHex robot are attached to an active driving joint, linking to the trunk, and produce a rotary motion on or in the

* Corresponding author.

E-mail address: liangding@hit.edu.cn (L. Ding).

Nomenclature

λ	Bulk density for specified particle type (N/m ³)
Δz	Intruding depth (m)
φ	Internal friction angle (°)
ϕ	External friction angle (°)
$\alpha_{1,2}$	Rising angles of Rankine active and passive zones (rad)
$h_{0,1}$	Height from plate apex to the free terrain surface and vertical length (m)
S	Contact area (m ²)
F_p	Mean passive pressure (N)
F_a	Mean active pressure (N)
β	Attack angle (rad)
γ	Intrusion angle (rad)
z	Ordinate in Cartesian coordinates of prescribed element (m)
F_z	Vertical contact net force (N)
F_x	Horizontal contact net force (N)
g	Acceleration due to gravity (N/kg)
r	Sagittal radius of sliding surface in polar coordinate (m)
r_0	Initial parameter determined by the attack angle β (m)
θ_r	Right boundary angle (rad)
G	Weight of sliding area (N)
F_s	Internal forces between consolidated part and sliding area (N)
F_l	Lateral pushing pressure/force (N)
F_p	Passive pressure exerted on sliding area (N)
d_p	Moment arm of passive pressure (m)
d_G	Moment arm of weight (m)
d_l	Moment arm of lateral pushing force (m)
x_G	Horizontal position of gravity center for sliding area (m)
θ	Included angle between horizontal plane and flat plate (rad)
x_B, z_B	Cartesian position of endpoint at right boundary condition (m)
b	Width of rectangular flat plate in three dimensions (m)
l	Length of rectangular flat plate in three dimensions (m)
A_s	Sliding area in side view (m ²)
A_{ss}	Logarithmic spiral sliding area in side view (m ²)
A_{st}	Triangular sliding area in side view (m ²)
d_{Gs}	Moment arm of weight for logarithmic spiral sliding area (m)
d_{Gt}	Moment arm of weight for triangular sliding area (m)
m	Sampling number in experimental data (dimensionless)
T	Transforming matrix (dimensionless)
l_{AB}	Length from rotary axis to plate element (m)
$F_{z,x}$	Vertical and horizontal contact net force (N)
x_p, z_p	Horizontal and vertical coordinates of point of application of contact force (m)
M	Net moment at point of application (N•m)
l_p	Length from point of application to rotary axis (m)
G_f	Weight of fan-shaped sliding part (N)
A_{sf}	Area of fan-shaped sector in side view (m ²)
d_{Gf}	Moment arm of fan-shaped sliding part (m)
d_{\perp}	Moment arm of normal component of passive pressure (m)
F_{pN}	Normal component of passive pressure (N)
F_{pT}	Tangential component of passive pressure (N)
b_e	Fitting width of sliding volume (m)
F_{lb}	Lateral force generated by the rising part (N)
G_b	Gravity of the rising part (N)
b_k	Ability to flow parameter (m)
a	Compressibility parameter (dimensionless)
ω_f	Volume fraction for particle aggregate (dimensionless)
M	Mass of particle aggregate (kg)
V	Volume of particle aggregate (m ³)

ρ_s	Particle grain density (N/m ³)
V_s	Volume of solid particle grain (m ³)
F_{pxi}, F_{pzi}	Horizontal and vertical passive forces at the i -th sampling attack angle point (N)
F_{expxi}, F_{expzi}	Experimental results versus the i -th attack angle sampling point (N)
Ψ_z	Goodness of fit for lift force (dimensionless)
Ψ_x	Goodness of fit for drag force (dimensionless)

granular substrates. While rotating around the joint, the foot penetrates the soil and reaches a deeper layer. Consequently, the interaction's mechanical responses change.

In trajectory planning [10], kinematic simulation [11], gait and stability control [12,13], and even in the structure design of locomotors [14], the role that interaction mechanics between locomotors and surrounding environments plays cannot be underestimated. Artificial environments for locomotors, common in human societies, are often designed to be rigid, flat, and non-slip. Rigid chain contact constraints are required in such environments [15]. TITAN-XI is an example of a series of quadruped robots that can walk on concrete slopes [16]. In contrast, off-road locomotion for legged robots is easily thwarted in natural environments [17] such as in deserts, tundra, and even extraterrestrial terrains [8]. An eccentric rotating paddle structure is employed in an amphibious-design robot when it swims in water [18], where the thrust force can be developed by hydrodynamics or fluid dynamics [9,19]. Conventionally, energy loss and continuity were the focus when using contact dynamics between mechanical systems [20,21]. Deformation and damping at different orientations are addressed in these models [22-25]. Some researchers hypothesized that contact occurs at the interface between elastic, viscoelastic [26], and viscoplastic [27,28] bodies without penetration into the ground. A nonlinear viscoplastic model has been developed to investigate the dynamic properties of a two-mass system for a prismatic hopping robot [27]. Hence, the viscoplastic model can be employed to build a controller capable of compensating for the energy loss on deformable terrains [28].

Terramechanic models proposed by Bekker et al. are developed to predict the stress distribution under wheeled or treaded vehicles on terrains [29,30]. They can also be employed to predict the contact forces between monopods and sand [11] in the continuum regime, using physical parameters such as foot dimensions [31] and cohesive and frictional moduli [32,33]. Hence, these parameters governing foot dimensions and soil properties have been measured and identified, which in part reveal the ability of robots to resist leg sinkage or tangential sliding [34,35]. However, this classical phenomenological model depicts contact forces during surface locomotion, which is less effective in predicting intrusion forces.

Fast-running animals and robots may impact their legs into granular media when they first touch down during each step. This is better explained by depth-dependent laws [36] that describe the lift and drag forces during high-speed, free-falling object impact [37]. However, during the majority of stance phases, their legs move relatively slowly, being forced (by the body) into granular media [9]. The resistive force theory was developed to better model legged locomotion on deformable ground, particularly for granular media [9]. It applies to slow, near quasi-static, forced intrusion and is based on stress-integral functions derived from an experimental analysis [9]. In addition, stagnant zone analyses under intruders of diverse shapes such as cones and semi-spheres have demonstrated that a modified Archimedes' law can explain intrusion forces in granular media [38]. Another contact model available in describing intruding locomotors is the passive earth pressure theory based on conventional soil mechanics [39,40]. In conventional soil mechanics, both Rankine and Coulomb theories are used to describe bearing forces on a retaining wall at a critical state and the soil behind it is assumed to be a semi-infinite body.



Fig. 1. Diagram of difference between the intrusion contact of lizard and surface contact of camel with sand particles, both types of interaction mechanisms have been implemented in legged robots, such as hexapod SandBot [5] and quadruped robots Bigdog [3]

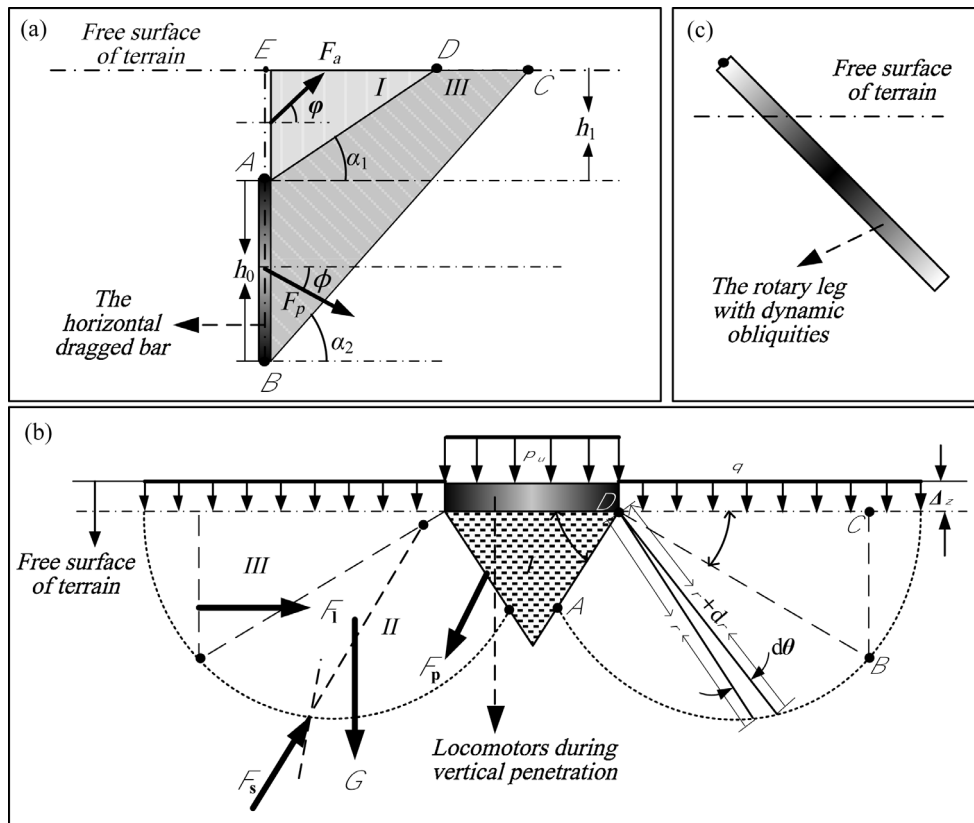


Fig. 2. Schematic principle of the Rankine zones for (a) dragged bar [41], (b) vertical penetrated locomotors [38], with flat surface and (c) their further extension to rotary legs.

Coulomb's theory differs from Rankine's in that it considers the effects of obliquity and friction on contact forces [39,40]. For a penetrated bar dragged at a low speed, the transitional zone II from I to III disappears and the boundary surface can be simplified as a straight line depending on Mohr-Coulomb failure criterion [41], as illustrated in Fig. 2(a). AB denotes the dragged bar surface, which can be regarded as a vertical leg with a flat surface. Without considering the resultant moment, the force of the failure state is achieved through maximization of the active force on the surface AD , and minimization of the passive force on the intersection surface BC [41]. Building upon the Coulomb sliding theory, Terzaghi hypothesized that the sliding surface for backfills was a logarithmic spiral [39], and his model has achieved a better prediction compared with the plane sliding surface assumption in Coulomb's theory. In geotechnical engineering, Terzaghi ultimate bearing capacity theory is primarily used to estimate the ultimate forces exerted on the soft terrains by foundations [39], which are normally laid on the terrain surface without inclinations. With regard to locomotors, the theory was employed by Kang et al. to predict the interaction forces between vertical penetrated flat locomotors with regular geometrical cross-sections such as rectangular, square, circular, triangular, etc., and particles [38] (shown in Fig. 2(b)). They also calibrated the calculation through an equivalent radius R' , defined as $R' = \sqrt{S/\pi}$, where S is the total area for these non-circular cross-sections. However, the issue of rotary locomotors encountering particles remains largely uninvestigated, as presented in Fig. 2(c).

Considering compact penetration beneath the surface [42], we chose Terzaghi's theory in our work because it describes continuous resisting forces at different obliquities exerted on structures with known particle parameters. However, it must be improved for application to legged locomotion, because the following assumptions made in the conventional Terzaghi theory are inapplicable for locomotors: 1) the retaining wall or other buildings are often assumed to have infinite width; 2) the analytical solution to the minimum passive force and center of gravity of the logarithmic spiral sliding section is difficult to achieve.

To establish the contact models between rotary locomotors and particles, we have improved the passive pressure model based on the sliding theory. A fitting width was proposed to represent the sliding volume in three dimensions and a spiral sliding approximation was addressed theoretically to emulate the sliding curve. The main contributions of this study lie in the highly physical description of the quasi-static constitutive contact process between locomotors and particles, and the excellent agreement between prediction results and experiments. Moreover, measurements of most conventional terramechanical parameters in this approach have been conducted in preceding studies, indicating that pre-identification is not required.

The remainder of this paper is divided into four parts. In Section 2, the preliminaries of the conventional sliding theory, motivation, and formulation of the problem are presented. Section 3 discusses our improvements to the sliding theory. In Section 4, the experimental apparatus and fitting results of the model are presented. Finally, Section 5 presents conclusions and future work.

2. Modeling based on Terzaghi bearing capacity theory: preliminaries

Two methods are often used to improve the legged locomotion performance: one is to optimize the algorithm that controls the motion through inverse dynamics [28], and the other is to conduct precise simulations [43]. However, compared with the continuum surroundings for legged robots, such as paved roads and marble hallways, dispersed particle substrates cannot provide sufficient resistance and propulsion for legged robots [44], resulting in a loss of performance. Although locomotors are not expected to intrude into the substrate, the legs are often semi-submerged by the particles in practice, especially in the rotary motion state [9,44]. Therefore, the interaction model between intruding legs and particles should be addressed.

As discussed in the previous section, Terzaghi’s ultimate bearing capacity theory can be employed to predict contact forces for either a horizontally dragged bar or rotary leg with a semi-ellipse configuration about one endpoint [41]. More significantly, a dominant variable in determining the resistive force is captured by a principle force, which can be obtained through failure-based derivations [41]. Scholars have also suggested that the Terzaghi model may be suitable for describing the contact of inclined wheel lugs of terrestrial vehicles, or even of the grousers at the bottom of tracked vehicles, with substrates [45].

In this section, the conventional passive pressure model is constructed using a logarithmic spiral yielding surface hypothesis [39]. Here the passive pressure is regarded as the contact force between rotary locomotors and substrates. Hence, we estimate the force borne by the immersed limb at each obliquity, associated with boundary conditions and continuity constructions. The results of the prediction and model fault are discussed.

2.1. Modeling process and pre-assumptions

The Prandtl-Reissner assumption, as the basis of Terzaghi’s theory, regards the sliding part as an entire body in a balanced status, leading to plastic deformations. It indicates that the inclined angle is $\pi/4 \pm \varphi/2$ for Rankine active and passive regions [39].

Assumption 1. Differing from translational motion, the Rankine active zone and uniform stress from the upper layer are neglected with regard to rotating locomotors. As illustrated in Fig. 3, a stationary rotating axis O is on the surface of a substrate, about which a flat plate is gradually rotated counterclockwise. The logarithmic spiral capturing the partly sliding surface is described by the arc OAB , tangential to a straight line BC at intersection point B . The entire Rankine zone is chosen to be the area $OABD$ and the particles beyond it are treated as solid regions. The spiral in sagittal planes [39] is expressed as follows:

$$r = r_0 \cdot \exp(\theta \tan \varphi) \tag{1}$$

where r denotes the distance from the spiral to origin dependent on the internal friction angle φ in polar coordinate; r_0 is the length of initial polar radius that rests with the attack angle β , and equal to the length of flat blade l if O is located at the terrain surface, as sketched in Fig. 3; θ is the rotary angle that the polar radii crosses over, revealed by the included

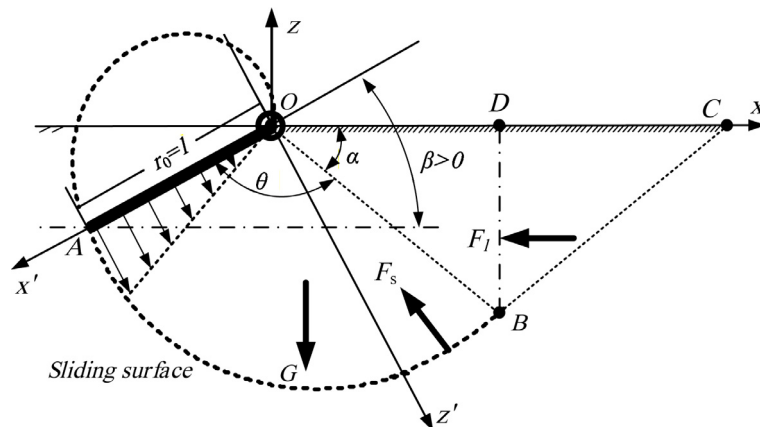


Fig. 3. Diagram of Terzaghi theory in describing the sliding area [39,47] between a rotary rectangular flat plate and granular substrates in side view.

angle between OA and OB in Fig. 3. There is a relation between the attack angle β and rotary angle θ for the blade OA governing by: $(\pi/4 - \varphi/2 + \theta + \beta) = \pi$.

As Fig. 3 depicts, the rightmost angle α , characterized as the right boundary, is $\pi/4 - \varphi/2$ (rad). The spiral-like stagnant area OAB and triangle OBD are balanced with both internal and external forces, composing of the gravity for sliding segment G , the internal forces F_s exerted on sliding part from the solid regime, the lateral pressure F_l , and the passive pressure F_p . Predictions are conducted through decomposition of F_p , an inversion to the drag and lift forces. Note that the force F_s passes through the origin O , and the net moment about the rotating axis is zero as a consequence of the combined effect of these four forces. The forward direction of the moment is set as counterclockwise, whereas the derived passive pressure is [39]

$$F_p = [F_l \cdot d_l + G \cdot d_G \cdot \text{sgn}(x_G)]/d_p \tag{2}$$

where d_p , d_G , and d_l denote the moment arms of forces F_p , G , and F_l , respectively, whereas x_G is the horizontal position of the center of gravity (COG) of the sliding region ($d_G = |x_G|$).

2.1.1. Boundary conditions of the sliding area

Calculating the weight and lateral forces, as well as their moment arms, requires two boundary conditions at critical state to be investigated in transient models within the Rankine active region.

- (1) Left boundary condition – contact interface between the leg and particles.

The left boundary condition is the interacting surface between the rotary leg and particles, indicated by the relation $r_0 = l$. Particularly, the endpoint A of the flat plate is passed by the logarithmic spiral.

- (2) Right boundary condition – Rankine passive zone

Here, the right boundary condition denotes the demarcation between the logarithmic spiral and Rankine passive regions, governed by the internal friction angle φ . When the included angle θ_r is specified to be

$$\theta_r = \pi - \beta - \left(\frac{\pi}{4} - \frac{\varphi}{2}\right) \tag{3}$$

The intersection point of the two sliding surfaces, represented by B , is located at

$$\begin{bmatrix} x_B \\ z_B \end{bmatrix} = l \cdot \exp(\theta_r \cdot \tan \varphi) \cdot \begin{bmatrix} \cos\left(\frac{\pi}{4} - \frac{\varphi}{2}\right) \\ -\sin\left(\frac{\pi}{4} - \frac{\varphi}{2}\right) \end{bmatrix} \tag{4}$$

where x_B and z_B represent the Cartesian position of B . The right boundary condition vanishes if β is greater than $\pi - \alpha$. The shapes and volumes for Rankine sliding zones, which are relevant to the lateral force, weight, and their moment arms, are dominated by both boundary conditions.

2.1.2. Lateral force and weight

The lateral pressure is primarily caused by the pushing effect in the horizontal direction, determined by the right boundary condition in Eq. (3). The left and right boundary conditions are both required in estimating the weight of the sliding part. If the effects of the aspect ratio of the stiffened substrates on the sliding geometrical wedge are ignored, the sliding region in three dimensions is approximated by a column. Hence, these particles cannot flow into the backfills, indicated by the upper left area of leg OA .

Without considering the width, the lateral pressure F_l is given as [39]

$$F_l = \frac{1}{2} \lambda z_b^2 \tan^2\left(\frac{\pi}{4} + \frac{\varphi}{2}\right) \tag{5}$$

where b is the width of the leg in three dimensions. Consequently, the weight of the sliding wedge is

$$G = \lambda A_s = \lambda \cdot (A_{AOB} + A_{OBD}) \tag{6}$$

where A_s indicates the sliding area in the side view (area $OABD$ in Fig. 3). A_s is composed of two areas, the spiral sector AOB and triangular one OBD (represented by A_{ABO} and A_{OBD}), which are calculated as

$$\begin{bmatrix} A_{AOB} \\ A_{OBD} \end{bmatrix} = \begin{bmatrix} \frac{1}{2} \int_0^{\theta_r} l^2 \cdot \exp(2\theta \cdot \tan \varphi) d\theta \\ \frac{1}{2} |x_B \cdot z_B| \end{bmatrix} \tag{7a}$$

$$= \begin{bmatrix} \frac{l^2}{4 \tan \varphi} [\exp(2\theta_r \cdot \tan \varphi) - 1] \\ l^2 \cdot \sin\left(\frac{\pi}{4} - \frac{\varphi}{2}\right) \cos\left(\frac{\pi}{4} - \frac{\varphi}{2}\right) \cdot \exp\left[2\left(\pi - \beta - \frac{\pi}{4} + \frac{\varphi}{2}\right) \cdot \tan \varphi\right] \end{bmatrix} \tag{7b}$$

From these dimensional parameters of the rectangular flat plate, including the width b and the length l , as well as the particle parameters, including the internal friction angle φ and the bulk density λ , the lateral pressure and weight can be obtained.

2.1.3. Point of application and force direction

The positions of the points of application of forces F_l , G , and F_p acting on the flat plate are prerequisites to obtaining the moment arms represented by d_p , d_G , and d_l , respectively.

2.1.3.1. Points of application and directions of lateral pushing force and passive earth pressure. The vector of the lateral force F_l is always horizontal, whereas the included angle between the passive pressure F_p vector and the normal vector of the plate surface is constant and is assumed to be the external frictional angle ϕ . The penetration leg is driven by the rotating force (torque) generated by the hip joint (or interpreted as the rotating axis), which is balanced by the torque generated by the counterforce of the passive pressure F_p . The points of application of F_p and F_l are considered to be acted upon at the lower one-third of the contact length [39].

$$\begin{bmatrix} d_p \\ d_l \end{bmatrix} = \frac{2}{3} \begin{bmatrix} l \cdot \cos \phi \\ |z_B| \end{bmatrix} = \frac{2}{3} \begin{bmatrix} l \cdot \cos \phi \\ l \cdot \exp \left[\left(\pi - \beta - \frac{\pi}{4} + \frac{\varphi}{2} \right) \cdot \tan \varphi \right] \cdot \sin \left(\frac{\pi}{4} - \frac{\varphi}{2} \right) \end{bmatrix} \quad (8)$$

2.1.3.2. Point of application of weight of sliding area. The point of application of weight G (center of mass, abbreviated as COM) will change owing to the rotary motion. The determination of the point of application requires both the information of the logarithmic spiral (OAB) COM and the right-angle triangle (OBD) COM. If the particles are uniformly distributed, the coordinates of the spiral COM in both the longitudinal and horizontal directions at local system $X'OZ'$ are calculated as

$$\begin{bmatrix} x'_{AOB} \\ z'_{AOB} \end{bmatrix} = \frac{1}{A_{AOB}} \left\{ \int_0^{\theta_t} \frac{2}{3} \cdot \frac{1}{2} [l \cdot \exp(\theta \tan \varphi)]^2 \cdot d\theta \cdot l \cdot \exp(\theta \tan \varphi) \cdot \begin{bmatrix} \cos \theta \\ \sin \theta \end{bmatrix} \right\} \quad (9)$$

The solution to Eq. (9) can be achieved through integration by parts (derived in the **Appendix**). The final COM should be obtained by transforming the results of Eq. (9) into that in the absolute coordinate XOZ .

$$\begin{bmatrix} x_{AOB} \\ z_{AOB} \end{bmatrix} = \begin{bmatrix} \cos(\pi - \beta) & \sin(\pi - \beta) \\ -\sin(\pi - \beta) & \cos(\pi - \beta) \end{bmatrix} \begin{bmatrix} x'_{AOB} \\ z'_{AOB} \end{bmatrix} \quad (10)$$

x_{AOB} is the final result of the weight arm. The above analysis is based on the precondition that $\beta < 3\pi/4 + \varphi/2$, which indicates that the logarithmic spiral sliding section exists. However, the passive force when $\beta > 3\pi/4 + \varphi/2$, indicating where the spiral sliding area has disappeared, would be discussed complementarily.

2.2. Problem for rotary locomotors using Terzaghi's theory

For vertical penetration, the normal force prediction based on the plastic sliding theory has been realized via a constitutive function of the sinkage Δz [38]. For rotary legs submerged into particles, contact models have been empirically established based on the resistive force theory [41]. It has been employed for predictions of the interaction force with the plastic failure criterion [41]. However, the force-deformation properties based on the sliding theory have not been fully investigated yet.

2.2.1. Preconditions in using Terzaghi's theory

The following preconditions should be satisfied in advance to theoretically describe the interaction process based on the sliding theory: 1) the status of the steady-state motion, which indicates a constant angular velocity is required to describe interaction forces; 2) a lateral sliding deformation, which indicates that no disturbance is produced along the width direction. At a low constant angular velocity (such as 0.2 rad/s [9,46]), its magnitude has a negligible influence on the interaction forces in experimental studies [41,46]. An estimated maximum rotational velocity of the leg that depends on the tolerance range of error should be determined. For example, 11 rad/s is recommended as the limit value in [41]. However, only less than 20% of the magnitude of the force is increased if the translational speed is increased from 0.01 to 1 m/s (with the corresponding angular velocity increased from 0.13 to 13.1 rad/s) for loosely packed particles [46].

2.2.2. Motivations of this research

In practice, rotation is a rather dynamic process with three variable Rankine zones. The contour of a Rankine active zone gradually blunts as the rotation proceeds. Consequently, several challenges arise when modeling the contact force based on the Terzaghi's sliding assumptions: 1) variations in the sliding section for both the side view and in three dimensions, and 2) the location of the zero moment point for rotary locomotors. We are focused on determining principles that can provide sufficient resistance to lateral rupture for legged locomotors, which are fundamental requirements for stabilized locomotion on granular media and relevant to the characteristics of the sliding parts. In practice, the plastic sliding principle for downward translational motion on particles is essentially the same as that for the rotation of the quasi-static status.

3. Modeling based on Terzaghi bearing capacity theory: improvements

From the above analysis, two aspects of the conventional Terzaghi model must be improved for further application to locomotors. These are 1) the volume of a sliding wedge in three dimensions dominated by the width as mentioned in Section 2.1.2; 2) the calculation method to achieve the analytical solution of the passive pressure, as well as the spiral sliding part, revealed in Section 2.1.3.

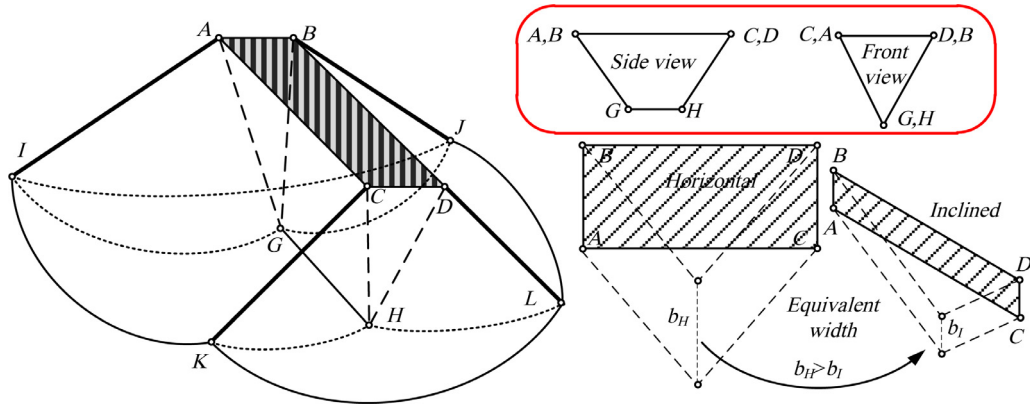


Fig. 4. Rankine zones beneath the flat plate situating in horizontal plane in two special occasions.

3.1. Improvement using a fitting width

In contrast to retaining walls where the width is often assumed to be of infinite length, the influence of width and aspect ratio on contact forces cannot be neglected for legged locomotors.

Because of the ability to flow and the angle of repose of particles, the sliding body generated by a rectangular leg is not exactly a column in three dimensions but a sliding wedge or a more complex body [39]. For a rectangular leg, the aspect ratio (b/l) and obliquity primarily affect the sliding volume in three dimensions [38,39]. If the rectangular flat plate is compressed vertically, the spatial geometry stagnant zone beneath the foot is a symmetric wedge, expressed as the cube $ABCDGH$, as illustrated in Fig. 4. Consequently, a single active stagnant zone and four couples of transitional and passive zones are generated. The value of the included angle between plate $ABCD$ and ABG or CDH , denoted by angle $\angle A$ or $\angle C$ in the side view, is $\pi/4 + \varphi/2$. It is equal to that between plate $ABCD$ and $ACHG$ or $BDHG$, denoted by the same angles in the front view. However, when the flat plate $ABCD$ is rotated about one single short side such as CD , the shape of the stagnant zone changes to an even pyramid, whose top and side views are shown in Fig. 4.

However, the intrusion length and obliquity of the rotary bar temporally changes. The volume of the Rankine active zone decreases as the horizontal rectangular flat plate is rotated to an inclination. A fitting width (indicated by b_H horizontally and b_I with obliquity, $b_H > b_I$) is required to adjust the sliding model to such an application because the following three physical parameters are difficult to predict and calculate.

- (1) The triggered variation in volume by longitudinal flows along the surface ABG and CDH ;
- (2) The volume of lateral sandy particles that pass by the lateral surfaces $ACHG$ and $BGHD$;
- (3) The coupled effects of gravity and arm for the backfills with regard to the rotary leg.

The magnitudes and variation trends in the contact force have been observed to be approached better through fitting two adjustable parameters: external frictional angle and width. Therefore, a fitting width is proposed to substitute the original width whereas the external frictional angle is modified through rotation experimental results.

Assumption 2. To simulate the actual sliding volume in three dimensions, we propose a fitting width indicated by b_e dominated by the attack angle β , that fully describes the volume variation of the Rankine passive zone:

$$b_e = b_k \cdot b \cdot a^{-\beta} \quad (11)$$

where b_k and a denote the parameters that are influenced by particle types and sizes, as well as the width and aspect ratio of rectangular flat blade. By replacing the leg width b with the fitting width b_e indicated by Eq. (11), the results are improved and closely approach the experimental data in calibration.

3.2. Improvement of zero moment point position

Concerning the rotating flat plate, a Terzaghi sliding surface is shown in Fig. 5 with the analytical image of the counter-clockwise rotary rectangular configured leg.

Assumption 3. The zero-moment point is located at the intersection of the leg and the terrain surface (represented by O).

Under the precondition of assumption 3, the gravity and lateral forces exerted on the sliding section should be further modified. If the flat plate is rotated within the transition region II, the following precondition must be satisfied:

$$\pi - \left(\frac{\pi}{4} - \frac{\varphi}{2} \right) > \beta > 0 \Rightarrow \frac{3\pi}{4} + \frac{\varphi}{2} > \beta > 0 \quad (12)$$

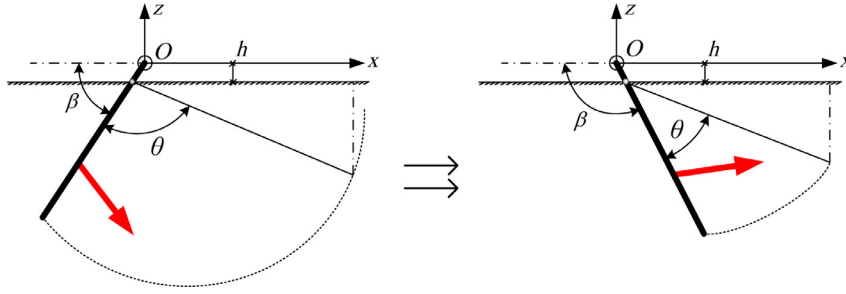


Fig. 5. Analytical image of a rotary rectangular flat plate with rotating axis fixed at the end point of O counterclockwise based on improved Terzaghi sliding surface.

Considering the left and right boundary conditions, as analyzed in Section 2.1, the central angle of the sliding part for transition region θ is given by

$$\theta = \frac{3\pi}{4} + \frac{\varphi}{2} - \beta \tag{13}$$

Subsequently, the weight of the logarithmic spiral sector G_{lg} , considering the width effect, is

$$G_{lg} = b_e \lambda \cdot \left(l - \frac{h}{\sin \beta} \right)^2 \frac{[\exp(2\theta \tan \varphi) - 1]}{4 \tan \varphi} \tag{14}$$

The moment arm of the spiral sliding region, d_{lg} , can be calculated as

$$d_{lg} = \left(l - \frac{h}{\sin \beta} \right) \frac{4 \tan \varphi \cdot f(\beta, \theta)}{3(1 + 9 \tan^2 \varphi) \cdot [\exp(2\theta \tan \varphi) - 1]} \tag{15}$$

where $f(\beta, \theta)$ is governed by the following expression:

$$f(\beta, \theta) = \sin \beta + 3 \tan \varphi \cos \beta + e^{3\theta \tan \varphi} \cdot [3 \tan \varphi \cos(\pi + \beta + \theta) - \sin(\beta + \theta)] \tag{16}$$

The weight of the triangular part, G_t , is

$$G_t = \frac{1}{4} b_e \lambda \left(l - \frac{h}{\sin \beta} \right)^2 \exp(2\theta \tan \varphi) \cos \varphi \tag{17}$$

Its corresponding moment arm, d_{tg} , is

$$d_{tg} = \frac{2}{3} \left(l - \frac{h}{\sin \beta} \right) \exp(\theta \tan \varphi) \cdot \cos \left(\frac{\pi}{4} - \frac{\varphi}{2} \right) \tag{18}$$

The lateral force and its moment arm are expressed as

$$\begin{bmatrix} F_l \\ d_l \end{bmatrix} = \begin{bmatrix} \frac{1}{2} \lambda b_e \left[\left(l - \frac{h}{\sin \beta} \right) \cdot \sin \left(\frac{\pi}{4} - \frac{\varphi}{2} \right) \exp(\theta \tan \varphi) \right]^2 \tan^2 \left(\frac{\pi}{4} + \frac{\varphi}{2} \right) \\ \frac{2}{3} \left(l - \frac{h}{\sin \beta} \right) \exp(\theta \tan \varphi) \cdot \sin \left(\frac{\pi}{4} - \frac{\varphi}{2} \right) \end{bmatrix} \tag{19}$$

Because the tangential force has no influence on the net moment, we only consider the moment arm d_{\perp} of the normal component of passive force. As another form of Eq. (2), the normal component of passive pressure F_{pN} is solved using

$$F_{pN} d_{\perp} = G_t d_{Gt} + F_l d_l + G_f d_{Gf} \tag{20}$$

Thus, the normal passive pressure is

$$[F_{pN}, d_{\perp}] = \left[\frac{1}{d_{\perp}} (G_t d_{Gt} + F_l d_l + G_f d_{Gf}), \frac{2}{3} \left(l - \frac{h}{\sin \beta} \right) \right] \tag{21}$$

The inverse matrix of the transforming matrix can be used to derive the vertical and horizontal forces.

$$F_{pT} = F_{pN} \cdot \tan \phi \tag{22a}$$

$$[F_z, F_x] = T^{-1} \cdot [F_{pN}, F_{pT}] \tag{22b}$$

where F_{pT} indicates the tangential component of passive pressure; T denotes the transforming matrix from local to absolute coordinate. At the excavating or raising motion state for legs, the intrusion angle is negative. Nevertheless, the presence of

the right boundary, as the division of Rankine passive zone into spiral and triangular sections, should be fully investigated. We obtain the central angle after the right boundary disappears:

$$\pi - \arcsin \frac{h}{l} > \beta > \pi - \left(\frac{\pi}{4} - \frac{\varphi}{2} \right) \quad (23)$$

Subsequently, the weight of the spiral sector and its moment arm are zero, but for the triangular sector,

$$[G_r, d_{Gr}] = \left[-\frac{1}{2}b\gamma \left(l - \frac{h}{\sin \beta} \right)^2 \sin \beta \cos \beta, -\frac{2}{3} \left(l - \frac{h}{\sin \beta} \right) \cdot \cos \beta \right] \quad (24)$$

The lateral force and its moment arm are expressed as

$$[F_l, d_l] = \left[\frac{1}{2}\lambda b \left[\left(l - \frac{h}{\sin \beta} \right) \cdot \sin \beta \right]^2 \tan^2 \left(\frac{\pi}{4} + \frac{\varphi}{2} \right), \frac{2}{3} \left(l - \frac{h}{\sin \beta} \right) \cdot \sin \beta \right] \quad (25)$$

When the rotary angle exceeds the right boundary, indicating that $\beta > 3\pi/4 + \varphi/2$, only the triangular sliding section is left. The above functions clearly indicate that the passive pressure is primarily influenced by the bulk density λ , and the internal and external friction angles φ and ϕ of the granular aggregate. The dimensional contributors of the rectangular flat plate include the initial inclined angle θ , length l , and width b . For specific particle types, the bulk density, the internal and external friction angles are all constants.

4. Results and discussions

Two experimental test groups with corresponding prediction results were performed, respectively. One involved measuring and predicting the drag and lift forces exerted on the legs, which are rotated in one particular substrate, for different width configurations; the other test group was performed using several particle types, but with a constant width.

4.1. Validation of the conventional sliding model for different widths

A testbed including a soil bin, industrial control system, and data acquisition system associated with its processing software, developed at Harbin Institute of Technology, was employed to determine the effects of the dimensions of a flat plate on the interaction model forms. The height of the free surface for sandy particles accommodated in the soil bin was adjusted according to the distance from the bottom of the leg to the solid foundation and the bottom of the soil bin. The dimensions of the soil bin was 1.8 m \times 1 m \times 1.5 m and the piezoelectricity signals were displayed on the monitor after filtrations. The details of the experimental apparatuses are shown in Fig. 6. Five detachable rotating flat plates of different widths ($b=20, 40, 60, 80, 100$ mm, as illustrated in Fig. 6), with the same length (250 mm) and thickness (4 mm), were designed in our testing groups, which are representative of a wide range of occasions. The bulk density of the test sand was 1.65×10^3 kg/m³ (the gravity per cubic meter was 16170 N/m³). The external frictional angle between the flat plate and sand was 0.3316 rad (19°).

The height of the rotary axis was fixed under the static balance of the jacking force, total weight of the system, and counterweights. The drag and lift forces were measured using a 6-dimensional F/T sensor, as shown in Fig. 6. Furthermore, the upper surface of the sand was smoothed by a scrapper after each test. The angular velocity was set to 0.12 rad/s to decrease the force vibrations as much as possible. The maximum intrusion depth was controlled to be 100 mm, achieved when the flat plate was vertical to the terrain surfaces.

The experimental results of the five width groups are shown in Fig. 7. Several conclusions can be drawn from the figures: 1) both the lift and drag forces increased as the width of the leg increased, but the peak lift force exhibited a more significant increase than the peak drag force; 2) the increments of passive forces also increased because the sandy particles were compressible, and some sandy particles were stacked and accumulated at the surface of the Rankine passive zone. Based on the traditional sliding model, the prediction results have been also illustrated in Fig. 7.

The accuracy of prediction results when $\beta > \pi/2$ is not discussed, because the contact forces were caused by the active sliding force instead of by the passive one. Furthermore, a small portion of the sliding particles accumulated at the upper surface of the passive region, which changed the gravity of the sliding section, the lateral force, and their arms. Using the conventional model, the variation trends were similar to the experimental results. However, there were poor agreements between the predictions based on the conventional sliding model and the experimental results.

4.2. Prediction results of the improved sliding model for different widths

If the average diameter of the testing particles, D , is much smaller than the width of flat plate b [47,48], governing by $b > 10D$, an accumulated rising part at different obliquities will be generated [47], marked by the red line shown in Fig. 8. Thus, the additional gravity and lateral force triggered by the rising part should be considered in the improved Terzaghi theory-based model [39].

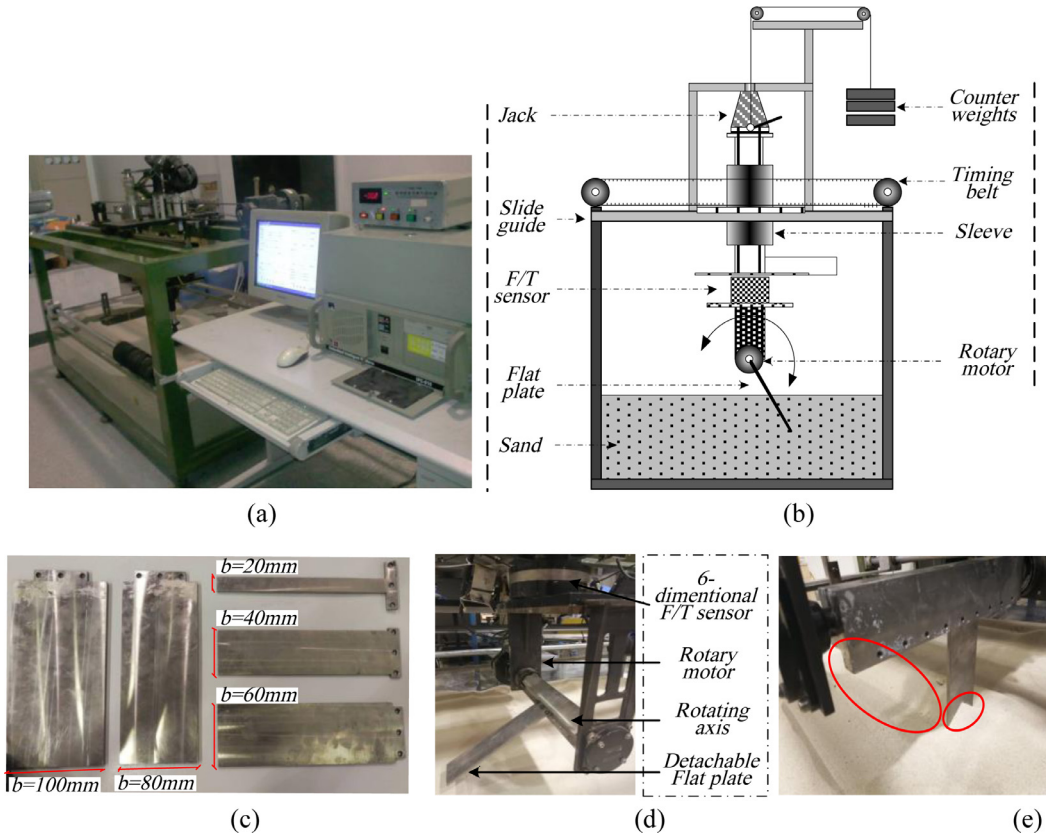


Fig. 6. Diagram of (a) the testbed for rotating flat plate with fixed rotary axis; (b) mechanical system; as well as the details of the rotary leg including: (c) the five width groups; (d) sensor, rotary motor/axis; and (e) subsided/stacked sand particles.

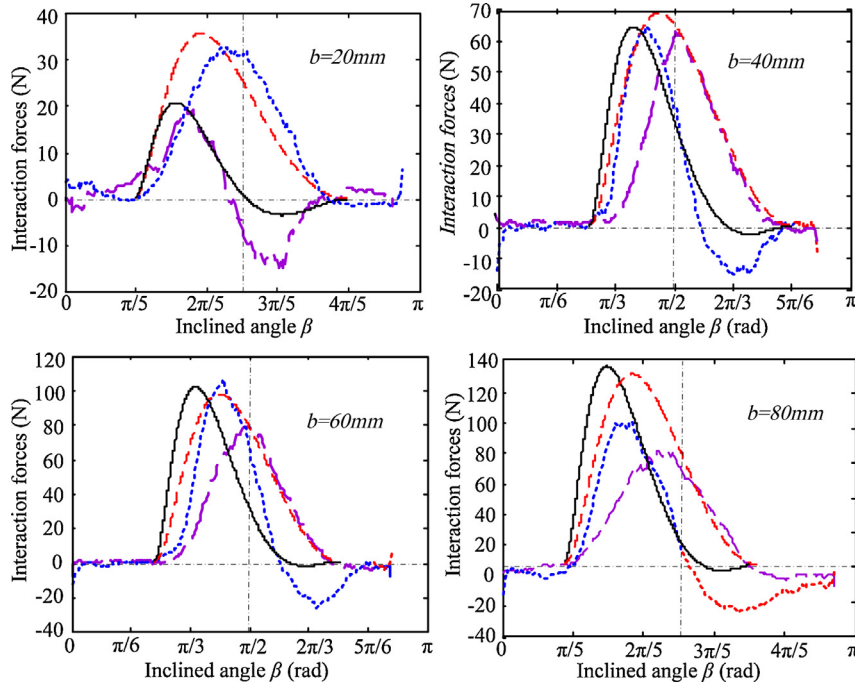


Fig. 7. Comparison of experimental and predicting results based on conventional sliding model, for the interaction forces between these flat plates with five different widths and sand.

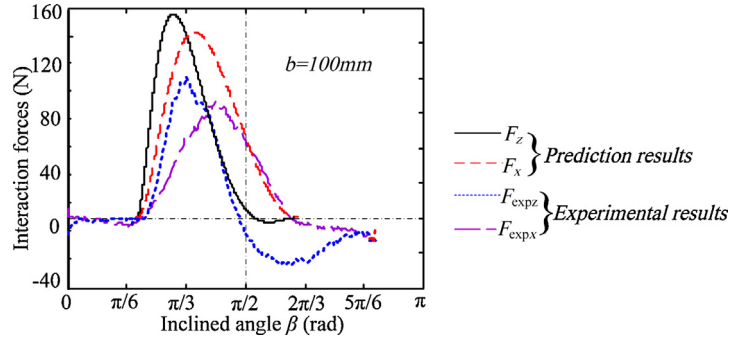


Fig. 7. Continued



Fig. 8. Accumulated rising parts at two different obliquities.

The volume of the rising section increased gradually as the rotation began, and then gradually decreased when the rotary flat plate was leaving the sand. In our improved Terzaghi model, the parameters b_k and a of fitting width, expressed as Eq. (11), were identified. The parameters are identified based on a linear regression to determine the optimal solution in Eq. (26).

$$\min_{\{b_k, a\}} \sum_{i=1}^m [(F_{pxi} - F_{expxi})^2 + (F_{pzi} - F_{expzi})^2] \tag{26}$$

where F_{pxi} and F_{pzi} denote the horizontal and vertical forces at the i -th attack angle point, respectively, whereas F_{expxi} and F_{expzi} are counterparts of F_{pxi} and F_{pzi} in the experiments, respectively. The experimental and prediction results are shown in Fig. 9. The prediction results were observed to not always be correct due to the accumulated rising section. Because robotic legs are designed to “step on” the terrain, we only considered the period when $\pi/2 > \beta > 0$. The fitting parameters and the goodness of fit are shown in Table 1. The goodness of fit for F_x after the model’s improvement was within the range of 91.09 to 97.25%, and that for F_z was within 92.83 to 98.32%, which reveals that there were well agreements between the prediction results and experimental data when $\beta < \pi/2$. As the leg width increases, both the values of parameters b_k and a will increase initially, to a critical magnitude, then gradually decrease. In the test groups, they have reached to the largest when leg width is 60mm, and the smallest when leg width $b = 20$ mm.

4.3. Validation of the conventional sliding model for different particle types

With the proposed fitting width, the improved Terzaghi model was also employed to predict the contact force between the flat plate and other particles. To test the improved Terzaghi theory, we used the experimental data of the interaction

Table 1 values of fitting parameters and goodness of fit at each width group when $0 < \beta < \pi/2$.

Leg width (mm)	Parameter b_k (dimensionless)	Parameter a (dimensionless)	Goodness of fit for F_x with improved model (%)	Goodness of fit for F_z with improved model(%)	Goodness of fit for F_x with conventional model (%)	Goodness of fit for F_z with conventional model (%)
20	0.24	0.26	94.72	97.49	67.52	47.84
40	4.45	1.61	91.09	97.52	58.27	62.74
60	22.40	7.78	94.86	96.19	37.31	43.26
80	11.06	5.31	97.25	98.32	27.91	29.05
100	6.66	3.58	94.40	92.83	12.11	10.74

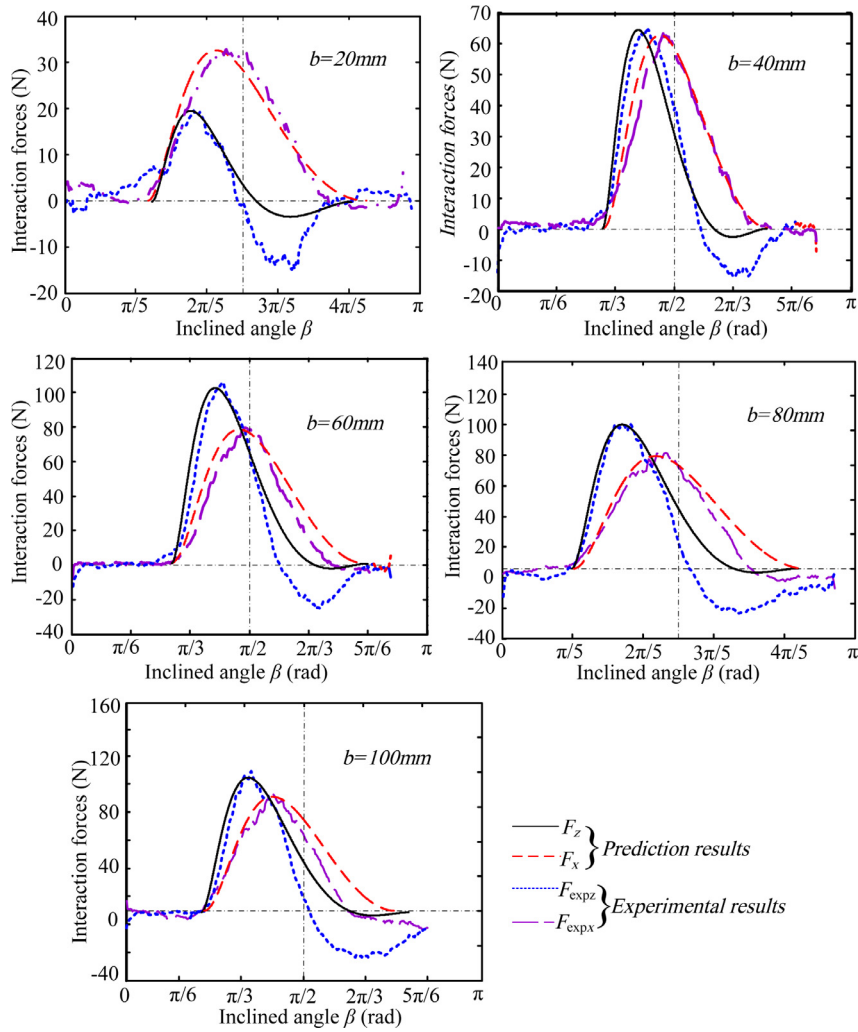


Fig. 9. Comparison of experimental and predicting results based on improved sliding model, for the interaction forces between these flat plates with five different widths and sand.

forces between particles and the flat plate in [9,46]. The derived unit weights of the aggregates and other physical parameters are listed in Table 2 [46].

$$\lambda = \frac{Mg}{V} = \frac{\rho_s V_s g}{V} = \rho_s g \omega_f \tag{27}$$

where ω_f denotes the volume fraction, M and V denote the mass and volume of particle aggregates respectively, g is the acceleration of gravity (here assumed to be 9.8 N/kg), and ρ_s and V_s indicate the particle grain density and solid volume, respectively. The internal friction angle ϕ was approximated by the angle of repose. The magnitude of the external friction

Table 2
Numerical values of physical parameters of experimental particles [9,46].

Particle types with their radius (mm)	Particle density ρ_s (kg/m ³)	Volume fraction ω_f (dimensionless)	Angle of repose (internal friction angle)	Estimated external friction angle between the aluminum legs and particles ϕ	Unit weight of aggregate λ (N/m ³)
LP poppy seeds	1.1×10^3	0.58	36°	$26^\circ \pm 1^\circ$	6.2524×10^3
CP poppy seeds	1.1×10^3	0.62	47°	$25^\circ \pm 1^\circ$	6.6836×10^3
LP glass beads	2.5×10^3	0.58	25°	$20^\circ \pm 1^\circ$	14.21×10^3
CP glass beads	2.5×10^3	0.62	35°	$21^\circ \pm 1^\circ$	15.19×10^3
CP glass spheres	2.6×10^3	0.63	21°	$18^\circ \pm 1^\circ$	16.05×10^3

*CP indicates “closely packed”; LP indicates “loosely packed”

Table 3
Numerical parameters using fitting width function of Eq. (11).

Identified parameter	Loosely packed poppy seed	Closely packed poppy seed	Loosely packed glass beads	Closely packed glass beads	Closely packed glass spheres
b_k	32.61	186.1	3.46	20.81	1.50
a	2.30	4.50	1.42	2.45	1.37

angle ϕ is well known to be dominated by the Coulomb friction coefficient μ when sliding occurs along a surface ($\tan\phi=\mu$). The legs encountering the particles were made from an aluminum product, characterized by light weight and smooth-surfaced properties. The common range of the friction coefficient in describing the Coulomb sliding friction between an aluminum body and another material ($\mu\approx 0.17\text{--}0.3$) [49] were used with the experimental data [9,46] ($F_T/F_N\approx\mu$, where F_N and F_T are the normal and tangential contact forces obtained through the Azimuth transformation of the vertical and horizontal forces $F_{x,z}$). The external friction angle between the legs and loosely packed glass spheres (polished compounds of silicon with spherical contours) was set at a constant value of $\phi\approx 20^\circ\pm 1^\circ$ in our calculations. The other estimated values of the external friction angles are listed in Table 2.

The prediction results based on the conventional Terzaghi theory are illustrated in Fig. 10. The angles of repose were used. The prediction results indicated that the master curve shapes for those five particles resembled each other. However, the errors between each simulated force and corresponding experimental results were large, resulting in poor experimental validation. The primary cause was that the contact was a mixture of elastic and plastic formulations. Other reasons are: 1) the actual aggregate of the stiffened particles when the plate was plunged into the particles (also interpreted as compressibility) and a few lateral particles were somewhat pushed away because of the flowability characteristics; and 2) while “excavating/raising”, many lateral particles were pushed away and spilled out, but the hardening of particles weakened to a large extent. Thus, to apply Terzaghi’s theory to modeling the interaction forces between locomotors and substrates, the model required to be further improved.

4.4. Prediction results of improved sliding model for different particle types

These identified parameters for particles are listed in Table 3.

Practically, the angle of repose indicates the measured maximum obliquity when particles begin to slide at a free surface under gravity and friction. In engineering practice, a small angle of repose indicates that the particles are highly flowable; the particles are difficult to slide if the angle of repose is large. Thus, the ability to flow of closely packed poppy seeds is poor, whereas loosely packed glass spheres slide easily. Quantitatively, the ability to flow can be determined by the magnitude of b_k —the smaller b_k is, the easier it is for the particles to flow. Moreover, the compressibility subject to resistive mechanics can be directly represented by the parameter a , for which greater compressibility leads to a larger parameter a .

By comparing the experimental and simulation results based on the improved Terzaghi ultimate bearing capacity theory indicated by the fitting width b_e , illustrated in Fig. 11, we observed that the simulation results in the improved Terzaghi model were much more accurate than those based on the conventional Terzaghi sliding assumption. To scale and calibrate

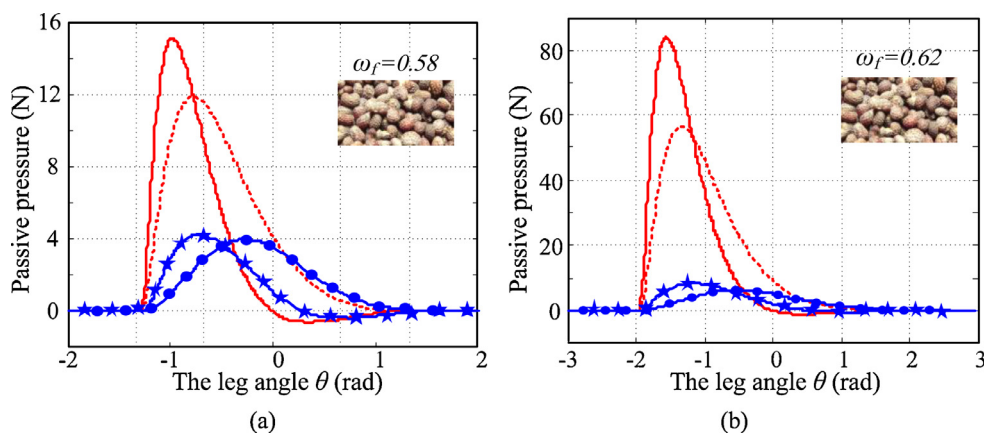


Fig. 10. Theoretical prediction results of horizontal and vertical components for contact passive pressure F_p in Eq. (2) based on conventional Terzaghi theory between rotating rectangular flat plate and (a) loosely packed poppy seeds, (b) closely packed poppy seeds, (c) loosely packed glass beads, (d) closely packed glass beads, and (e) closely packed glass spheres. Experimental data are from [9,46].

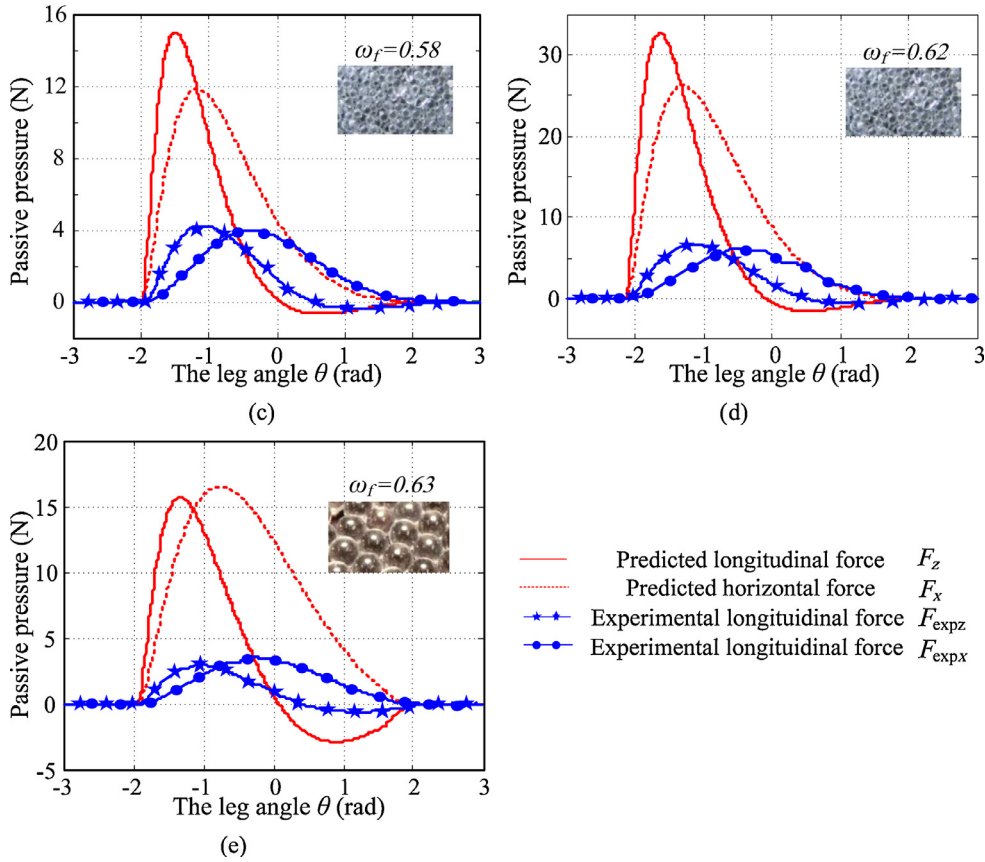


Fig. 10. Continued

the goodness of fit for the prediction model, two indices were estimated:

$$\Psi_{x,z} = 1 - \left\{ \sum_{i=1}^m (F_{pxi,zi} - F_{expxi,zi})^2 \right\} / \left(\sum_{i=1}^m F_{expxi,zi}^2 \right) \quad (28)$$

where $\Psi_{x,z}$ denotes the goodness of fit in prediction, m the total number of experimental data, and $F_{pxi,zi}$, $F_{expxi,zi}$ the horizontal and vertical passive pressures in predictions and experiments, respectively.

The goodness of fit for these five types of particles is presented in Table 4. The minimum goodness of fit for the vertical and horizontal forces were 90.32 and 93.85%, respectively, which occurred at the interface with the loosely packed glass spheres.

4.5. Discussions

Regardless of the change in the width and particle types, the prediction results can be optimized using such a simplified fitting width. The results of this paper can still be applied to other scenarios with analogous leg dimensions (e.g., aspect ratio and materials), motion status (e.g., angular velocity and location of the rotation point), and particle types (e.g., void ratio and particle size).

Table 4
Goodness of fit for the improved Terzaghi model.

Goodness of fit in prediction (%)	Loosely packed poppy seed	Closely packed poppy seed	Loosely packed glass spheres	Closely packed glass spheres	Closely packed glass spheres
Ψ_z	99.05	99.19	98.65	98.49	95.88
Ψ_x	97.46	98.46	97.63	99.22	92.50

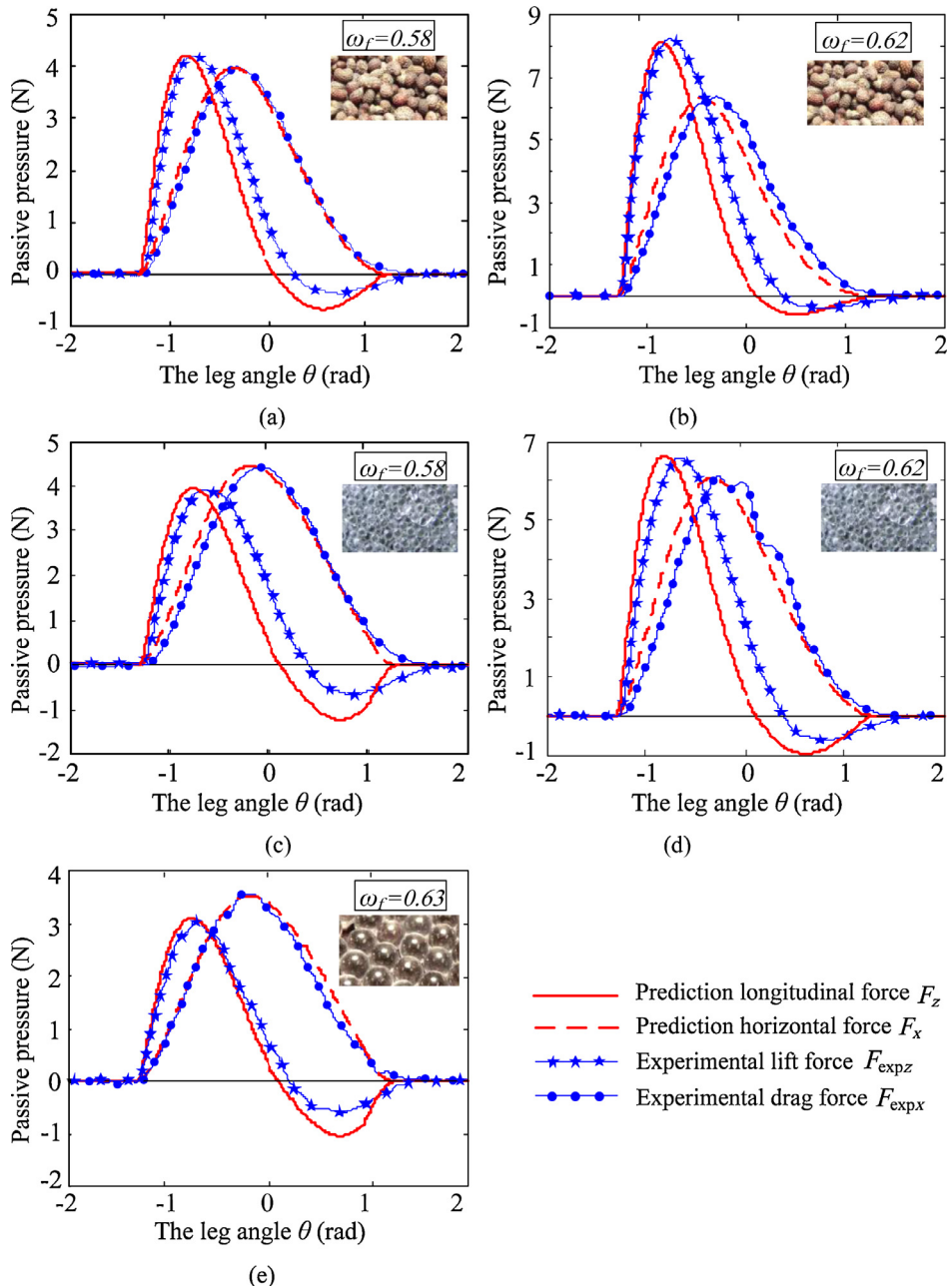


Fig. 11. Prediction results of the improved Terzaghi model with the fitting width and experiments results between rotating rectangular flat plate and five particles: (a) loosely and (b) closely packed poppy seeds, (c) loosely and (d) closely packed glass beads with particle diameters of 0.3 mm, and (e) closely packed glass spheres with particle diameters of 3 mm. Experimental data are from [9,46].

5. Conclusions and future work

In this study, an improved Terzaghi theory based on a fitting width was developed to model the contact process between a rectangular flat plate of various dimensions and granular particles of different types. The results of this paper can be applied to other scenarios such as the amphibious legged locomotion, mining on the Earth, or extraterrestrial explorations.

- (1) Our work has broadened the applicability of conventional soil mechanics models and has elucidated on practical fields of penetration locomotors.

- (2) Based on the fitting width and the determination of their parameters, our model achieved an excellent predictive capability of forces on robotic legs rotating in granular media. This indicated that Terzaghi's original assumptions are feasible in describing interaction forces for locomotors.
- (3) The improved Terzaghi model is sensitive to the internal friction angle and bulk density of granular media, which indicates that the model can help characterize these physical parameters if the contact forces and moving position are obtained through robotic sensors [50]. The magnitudes of these physical parameters are available in terramechanics literature, making these previous measurements directly useful for our model. In addition, such a macroscopic model does not necessarily require the details of stress, which can reduce the calculation effort. These parameters in the fitting width can be employed to indicate the properties of compressibility and ability to flow of particles.
- (4) In the research and development phase, the contact force models can be used in the design and performance analysis of immersed penetration robotic legs with these terramechanic parameters from literature. In the operation phase, the parameters of the models can be identified online to improve accuracy and fidelity.

In the future, the model should be generalized by considering the following: the effects of more complex shapes and composite structures in the design of penetration locomotors on the ability of compressibility and flow; possible variation in fitted parameters such as the aspect ratio, thickness, or even the granular materials; and improvement if substrates comprise cohesive particles [51].

Funding

This study was supported in part by the [National Natural Science Foundation of China](#) (grant no. 51822502 and 91948202), the [Foundation for Innovative Research Groups of the National Natural Science Foundation of China](#) (grant no. 51521003), the [Fundamental Research Funds for the Central Universities](#) (grant no. HIT.BRETIV.201903), and the "111 Project" (grant no. B07018).

Declaration of Competing Interest

The authors declare that they have no known competing financial interests or personal relationships that could have appeared to influence the work reported in this paper.

Acknowledgment

We thank Daniel I. Goldman for sharing experimental data collected in his laboratory.

Appendix

The arm of gravity is derived thus:

$$\frac{1}{A_{AOB}} \left\{ \int_0^{\theta_r} \frac{2}{3} \cdot \frac{1}{2} [l \cdot \exp(\theta \tan \varphi)]^2 \cdot d\theta \cdot l \cdot \exp(\theta \tan \varphi) \cdot \begin{bmatrix} \cos \theta \\ \sin \theta \end{bmatrix} \right\} \tag{A1}$$

$$= \frac{l^3}{3A_{AOB}} \left\{ \int_0^{\theta_r} [\exp(3\theta \tan \varphi)] \cdot \begin{bmatrix} \cos \theta \\ \sin \theta \end{bmatrix} d\theta \right\} \tag{A2}$$

$$= \frac{1}{3A_{AOB}} \left\{ \int_0^{\theta_r} [l \cdot \exp(\theta \tan \varphi)]^3 d \begin{bmatrix} \sin \theta \\ -\cos \theta \end{bmatrix} \right\} \tag{A3}$$

$$= \frac{1}{3A_{AOB}} \left\{ [l \cdot \exp(\theta_r \tan \varphi)]^3 \begin{bmatrix} \sin \theta_r \\ -\cos \theta_r \end{bmatrix} - l^3 \begin{bmatrix} 0 \\ -1 \end{bmatrix} - \int_0^{\theta_r} \begin{bmatrix} \sin \theta \\ -\cos \theta \end{bmatrix} d[l \cdot \exp(\theta \tan \varphi)]^3 \right\} \tag{A4}$$

$$= \frac{1}{3A_{AOB}} \left\{ [l \cdot \exp(\theta_r \tan \varphi)]^3 \begin{bmatrix} \sin \theta_r \\ -\cos \theta_r \end{bmatrix} - l^3 \begin{bmatrix} 0 \\ -1 \end{bmatrix} - l^3 \cdot \int_0^{\theta_r} \begin{bmatrix} \sin \theta \\ -\cos \theta \end{bmatrix} d[\exp(3\theta \tan \varphi)] \right\} \tag{A5}$$

$$= \frac{1}{3A_{AOB}} \left\{ [l \cdot \exp(\theta_r \tan \varphi)]^3 \begin{bmatrix} \sin \theta_r \\ -\cos \theta_r \end{bmatrix} - l^3 \begin{bmatrix} 0 \\ -1 \end{bmatrix} - 3l^3 \tan \varphi \cdot \int_0^{\theta_r} \exp(3\theta \tan \varphi) \cdot \begin{bmatrix} \sin \theta \\ -\cos \theta \end{bmatrix} d\theta \right\} \tag{A6}$$

$$= \frac{1}{3A_{AOB}} \left\{ [l \cdot \exp(\theta_r \tan \varphi)]^3 \begin{bmatrix} \sin \theta_r \\ -\cos \theta_r \end{bmatrix} - l^3 \begin{bmatrix} 0 \\ -1 \end{bmatrix} - 3l^3 \tan \varphi \cdot \int_0^{\theta_r} \exp(3\theta \tan \varphi) \cdot d \begin{bmatrix} -\cos \theta \\ -\sin \theta \end{bmatrix} \right\} \tag{A7}$$

$$= \frac{1}{3A_{AOB}} \left\{ [l \cdot \exp(\theta_r \tan \varphi)]^3 \begin{bmatrix} \sin \theta_r \\ -\cos \theta_r \end{bmatrix} - l^3 \begin{bmatrix} 0 \\ -1 \end{bmatrix} \right\} - \frac{l^3 \tan \varphi}{A_{AOB}} \cdot \int_0^{\theta_r} \exp(3\theta \tan \varphi) \cdot d \begin{bmatrix} -\cos \theta \\ -\sin \theta \end{bmatrix} \tag{A8}$$

$$= \frac{1}{3A_{AOB}} \left\{ [l \cdot \exp(\theta_r \tan \varphi)]^3 \begin{bmatrix} \sin \theta_r \\ -\cos \theta_r \end{bmatrix} - l^3 \begin{bmatrix} 0 \\ -1 \end{bmatrix} \right\} - \frac{l^3 \tan \varphi}{A_{AOB}} \cdot \left\{ -\exp(3\theta_r \tan \varphi) \begin{bmatrix} \cos \theta_r \\ \sin \theta_r \end{bmatrix} - \begin{bmatrix} -1 \\ 0 \end{bmatrix} - \int_0^{\theta_r} \begin{bmatrix} -\cos \theta \\ -\sin \theta \end{bmatrix} \cdot d \exp(3\theta \tan \varphi) \right\} \quad (A9)$$

$$= \frac{1}{3A_{AOB}} \left\{ [l \cdot \exp(\theta_r \tan \varphi)]^3 \begin{bmatrix} \sin \theta_r \\ -\cos \theta_r \end{bmatrix} - l^3 \begin{bmatrix} 0 \\ -1 \end{bmatrix} \right\} + \frac{l^3 \tan \varphi}{A_{AOB}} \cdot \left\{ \exp(3\theta_r \tan \varphi) \begin{bmatrix} \cos \theta_r \\ \sin \theta_r \end{bmatrix} + \begin{bmatrix} -1 \\ 0 \end{bmatrix} - 3 \tan \varphi \cdot \int_0^{\theta_r} \begin{bmatrix} \cos \theta \\ \sin \theta \end{bmatrix} \cdot \exp(3\theta \tan \varphi) d\theta \right\} \quad (A10)$$

$$= \frac{1}{3A_{AOB}} \left\{ [l \cdot \exp(\theta_r \tan \varphi)]^3 \begin{bmatrix} \sin \theta_r \\ -\cos \theta_r \end{bmatrix} - l^3 \begin{bmatrix} 0 \\ -1 \end{bmatrix} \right\} + \frac{l^3 \tan \varphi}{A_{AOB}} \cdot \left\{ \exp(3\theta_r \tan \varphi) \begin{bmatrix} \cos \theta_r \\ \sin \theta_r \end{bmatrix} + \begin{bmatrix} -1 \\ 0 \end{bmatrix} \right\} - \frac{3l^3 \tan^2 \varphi}{A_{AOB}} \cdot \int_0^{\theta_r} \exp(3\theta \tan \varphi) \cdot \begin{bmatrix} \cos \theta \\ \sin \theta \end{bmatrix} d\theta \quad (A11)$$

Note that

$$\left\{ \int_0^{\theta_r} [\exp(3\theta \tan \varphi)] \cdot \begin{bmatrix} \cos \theta \\ \sin \theta \end{bmatrix} d\theta \right\} = \left\{ \exp(3\theta_r \tan \varphi) \begin{bmatrix} \sin \theta_r \\ -\cos \theta_r \end{bmatrix} - \begin{bmatrix} 0 \\ -1 \end{bmatrix} \right\} + 3 \tan \varphi \cdot \left\{ \exp(3\theta_r \tan \varphi) \begin{bmatrix} \cos \theta_r \\ \sin \theta_r \end{bmatrix} + \begin{bmatrix} -1 \\ 0 \end{bmatrix} \right\} - 9 \tan^2 \varphi \cdot \int_0^{\theta_r} \exp(3\theta \tan \varphi) \cdot \begin{bmatrix} \cos \theta \\ \sin \theta \end{bmatrix} d\theta \quad (A12)$$

Thus, Eq. (A12) can be transformed into:

$$(1 + 9 \tan^2 \varphi) \left\{ \int_0^{\theta_r} [\exp(3\theta \tan \varphi)] \cdot \begin{bmatrix} \cos \theta \\ \sin \theta \end{bmatrix} d\theta \right\} = \left\{ \exp(3\theta_r \tan \varphi) \begin{bmatrix} \sin \theta_r \\ -\cos \theta_r \end{bmatrix} - \begin{bmatrix} 0 \\ -1 \end{bmatrix} \right\} + 3 \tan \varphi \cdot \left\{ \exp(3\theta_r \tan \varphi) \begin{bmatrix} \cos \theta_r \\ \sin \theta_r \end{bmatrix} + \begin{bmatrix} -1 \\ 0 \end{bmatrix} \right\} \quad (A13)$$

Whereas

$$\int_0^{\theta_r} [\exp(3\theta \tan \varphi)] \cdot \begin{bmatrix} \cos \theta \\ \sin \theta \end{bmatrix} d\theta = \frac{1}{1+9 \tan^2 \varphi} \left\{ \exp(3\theta_r \tan \varphi) \begin{bmatrix} \sin \theta_r \\ -\cos \theta_r \end{bmatrix} - \begin{bmatrix} 0 \\ -1 \end{bmatrix} \right\} + \frac{3 \tan \varphi}{1+9 \tan^2 \varphi} \cdot \left\{ \exp(3\theta_r \tan \varphi) \begin{bmatrix} \cos \theta_r \\ \sin \theta_r \end{bmatrix} + \begin{bmatrix} -1 \\ 0 \end{bmatrix} \right\} \quad (A14)$$

The final result of Eq. (A2) is:

$$\frac{l^3}{3A_{AOB}} \left\{ \int_0^{\theta_r} [\exp(3\theta \tan \varphi)] \cdot \begin{bmatrix} \cos \theta \\ \sin \theta \end{bmatrix} d\theta \right\} = \frac{l^3}{3A_{AOB}} \left\{ \exp(3\theta_r \tan \varphi) \begin{bmatrix} \sin \theta_r \\ -\cos \theta_r \end{bmatrix} - \begin{bmatrix} 0 \\ -1 \end{bmatrix} \right\} + \frac{l^3 \tan \varphi}{A_{AOB}} \cdot \left\{ \exp(3\theta_r \tan \varphi) \begin{bmatrix} \cos \theta_r \\ \sin \theta_r \end{bmatrix} + \begin{bmatrix} -1 \\ 0 \end{bmatrix} \right\} - \frac{3l^3 \tan^2 \varphi}{A_{AOB}} \cdot \int_0^{\theta_r} \exp(3\theta \tan \varphi) \cdot \begin{bmatrix} \cos \theta \\ \sin \theta \end{bmatrix} d\theta \quad (A15)$$

References

- [1] R. Siegwart, L.R. Nourbakhsh, D. Scaramuzza, Introduction to autonomous mobile robots, Intelligent Robotics and Autonomous Agents series, The MIT Press, Massachusetts Institute of Technology, Cambridge, Massachusetts, 2004 ISBN 0-262-01535-8.
- [2] A.Y. Holly, N. Adam, O. Willard, S. David, S. Anna, V. Jack, Analysis of human-robot interaction at the DARPA robotics challenge trial, J. Field Rob. 32 (3) (2015) 420–444.
- [3] R. Playter, M. Buehler, M. Raibert, Bigdog, in: Proceedings of International Society for Optical Engineering, 2006, pp. 1–6.
- [4] F.F. Qian, T.N. Zhang, W. Korff, P.B. Umbanhowar, R.J. Full, D.I. Goldman, Principles of appendage design in robots and animals determining terradynamic performance on flowable ground, Bioinspiration Biomim. 10 (5) (2015) 056014.
- [5] D. Goldman, H. Komsuoglu, D. Koditschek, March of the SandBots, Spectr. IEEE 46 (4) (2009) 30–35.
- [6] U. Saranli, M. Buehler, D.E. Koditschek, RHEx: a simple and highly mobile hexapod robot, Int. J. Robot. Res. 20 (7) (2001) 616–631.
- [7] R. Altendorfer, N. Moore, H. Komsuoglu, M. Buehler, J.R. Brown, H.B. Mcmordie, D. Saranli, U. Full, R. Koditschek, RHEx: a biologically inspired hexapod runner, Auton. Robots 11 (3) (2001) 207–213.
- [8] C. Li, P.B. Umbanhowar, H. Komsuoglu, D.E. Koditschek, D.I. Goldman, Sensitive dependence of the motion of a legged robot on granular media, Proc. Natl. Acad. Sci. U. S. Am. (PNAS) 106 (9) (2009) 3029–3034.
- [9] C. Li, T.N. Zhang, D.I. Goldman, A terradynamics of legged locomotion on granular media, Science 339 (6126) (2013) 1408–1411.
- [10] C.M. Hubicki, J.J. Aguilar, D.I. Goldman, A.D. Ames, Tractable terrain-aware motion planning on granular media: an impulsive jumping study, in: IEEE/RSJ International Conference on Intelligent Robots & Systems, 2016, pp. 3887–3892.
- [11] L. Ding, H.B. Gao, Z.Q. Deng, J.H. Song, Y.Q. Liu, G.J. Liu, K. Iagnemma, Foot-terrain interaction mechanics for legged robots: modeling and experimental validation, Int. J. Robot. Res. 32 (13) (2013) 1585–1606.

- [12] C. Gong, M.J. Travers, H.C. Astley, L. Li, J.R. Mendelson, D.I. Goldman, H. Choset, Kinematic gait synthesis for snake robots, *Int. J. Robot. Res.* (2015) 1–14.
- [13] H.F.N. Al-Shuka, F. Allmendinger, B. Corves, W.H. Zhu, Modeling, stability and walking pattern generators of biped robots: a review, *Robotica* 32 (6) (2014) 907–934.
- [14] M. Kwan, M. Hubbard, Optimal foot shape for a passive dynamic biped, *J. Theor. Biol.* 248 (2007) 331–339.
- [15] S. Zapolosky, E. Drumwright, Inverse dynamics with rigid contact and friction, *Auton. Robots* 41 (2017) 831–863.
- [16] R. Hodoshima, T. Doi, Y. Fukuda, S. Hirose, T. Okamoto, J. Mori, Development of TITAN XI: a quadruped walking robot to work on slopes, in: *Proceedings of 2004 IEEE/RSJ International Conference on Intelligent Robots and Systems*, 2004, pp. 792–797.
- [17] Y. Yin, S. Rakheja, P.E. Boileau, A roll stability performance measure for off-road vehicles, *J. Terramech.* 64 (2016) 58–68.
- [18] Sun, Y., Ma, S., Fujita, K., Yang, Y., Pu, H., “Modeling the rotational paddling of an ePaddle-based amphibious robot,” 2012IEEE/RSJ International Conference on Intelligent Robots and Systems, Vilamoura, Algarve, Portugal, 610–615.
- [19] Anderson, J.D., “Computational Fluid Dynamics,” McGraw-Hill Education, ISBN-13: 978-0070016859.
- [20] G. Gilardi, I. Sharf, Literature survey of contact dynamics modelling, *Mech. Mach. Theory* 37 (2002) 1213–1239.
- [21] A. Tornambe, Modeling and control of impact in mechanical systems: theory and experimental results, *IEEE Trans. Autom. Control* 44 (2) (1999) 294–309.
- [22] L. Biagiotti, C. Melchiorri, P. Tiezzi, G. Vassura, Modelling and identification of soft pads for robotic hands, in: *IEEE/RSJ International Conference on Intelligent Robots & Systems*, 2005, pp. 2786–2791.
- [23] M. Webber, O. Ma, I. Sharf, Identification of contact dynamics model parameters from constrained robotic operations, *J. Dyn. Sys., Meas., Control* 128 (2) (2005) 307–318.
- [24] A. Haddadi, K. Hashtrudi-Zaad, Online contact impedance identification for robotic systems, in: *IEEE/RSJ International Conference on Intelligent Robots & Systems*, 2008, pp. 22–26.
- [25] T. Piatkowski, Dahl and LuGre dynamic friction models – the analysis of selected properties, *Mech. Mach. Theory* 73 (2) (2014) 91–100.
- [26] V.L. Popov, in: *Contact Mechanics And Friction-Physical Principles and Applications*, Springer-Verlag, Berlin, Heidelberg, Chap. 2010, p. 2. ISBN 978-3-642-10802-0.
- [27] D.A. Jacobs, *Efficient, Stable Locomotion in Legged Robots* PhD Thesis, Dept. of Mech. Engineering, Stanford University, 2012.
- [28] V. Vasilopoulos, I.S. Paraskevas, E.G. Papadopoulos, Compliant terrain legged locomotion using a viscoplastic approach, in: *2014 IEEE/RSJ International Conference on Intelligent Robots and Systems (IROS 2014)*, Chicago, IL, 2014, pp. 14–18. September.
- [29] Sh. Taheri, C. Sandu, S. Taheri, E. Pinto, D. Gorsich, A technical survey on Terramechanics models for tire-terrain interaction used in modeling and simulation of wheeled vehicles, *J. Terramech.* 57 (2014) 1–22.
- [30] G. Ishigami, A. Miwa, K. Nagatani, K. Yoshida, Terramechanics-based model for steering maneuver of planetary exploration rovers on loose soil, *J. Field Rob.* 24 (3) (2007) 233–250.
- [31] M. Spenko, M. Cutkosky, C. Majidi, R. Fearing, R. Groff, K. Autumn, Foot design and integration for bioinspired climbing robots, *Proc. of SPIE* 6230 (623019) (2006) 1–12.
- [32] M.A. Hoepflinger, C.D. Remy, M. Hutter, L. Spinello, R. Siegwart, Haptic terrain classification for legged robots, *IEEE Int. Conf. Robot. Autom.* 58 (8) (2010) 2828–2833.
- [33] P. Dallaire, K. Walas, P. Giguere, B. Chaib-draa, Learning terrain types with the Pitman-Yor process mixtures of gaussians for a legged robot, in: *IEEE/RSJ International Conference on Intelligent Robots & Systems*, 2015, pp. 3457–3463.
- [34] M.G. Bekker, *The Theory of Land Locomotion*, University of Michigan Press, Ann Arbor, Michigan, 1956.
- [35] J.Y. Wong, A.R. Reece, Prediction of Rigid Wheel Performance Based on Analysis of Soil-Wheel Stresses, *J. Terramech.* 4 (1) (1967) 81–98.
- [36] T. Brzinski III, P. Mayor, D. Durian, Depth-dependent resistance of granular media to vertical penetration, *Phys. Rev. Lett.* 111 (16) (2013) 168002.
- [37] H. Katsuragi, D. Durian, Unified force law for granular impact cratering, *Nat. Phys.* 3 (2007) 420–423.
- [38] W. Kang, Y. Feng, C. Liu, R. Blumenfeld, Archimedes’ law explains penetration of solids into granular media, *Nat. Commun.* (2018), doi:10.1038/s41467-0.18-03344-3.
- [39] K. Terzaghi, R.B. Peck, G. Mesri, *Soil Mechanics in Engineering Practice*, A Wiley-Interscience Publication, JOHN WILEY & SONS, INC, New York, Chichester, Brisbane, Toronto, Singapore, 1996 ISBN 0-471-08658-4.
- [40] K. Terzaghi, *Theoretical Soil Mechanics*, Wiley and Sons, New York, 1943, doi:10.1002/9780470172766.
- [41] L. Xu, S. Zhang, N. Jiang, R. Xu, A hybrid force model to estimate the dynamics of curved legs in granular material, *J. Terramech.* 59 (2015) 59–70.
- [42] M.L. Hunt, Robotic walking in the real world, *Science* 339 (6126) (2013) 1389–1390.
- [43] H. Gao, M. Jin, L. Ding, Y. Liu, W. Li, et al., A real-time, high fidelity dynamic simulation platform for Hexapod robots on soft terrain, *Simul. Model. Pract. Theory* 68 (2016) 125–145.
- [44] M.F. Chang, Lateral earth pressures behind rotating walls, *Can. Geotech. J.* 34 (4) (1997) 498–509.
- [45] J.Y. Wong, *Theory of Ground Vehicle*, 4th edition, John Wiley & Sons, New York, 2008.
- [46] Li, C., Zhang, T. N., Goldman, D. I., 2013, *Supplementary Materials for "A terradynamics of legged locomotion on granular media"*.
- [47] G.X. Li, B.Y. Zhang, Y.Z. Yu, *Soil Mechanics*, 2nd edition, Tsinghua University Press, 2013 ISBN: 9787302331766.
- [48] K.J. Zhang, *Vehicle-Terramechanics*, National Defence Industry Press, 2002 ISBN: 9787118025644.
- [49] D.X. Cheng, et al., *Handbook of Mechanical Design*, Chemical Industry Press, 2008 ISBN: 978-7-122-01408-5.
- [50] F. Qian, D.B. Lee, S. Bodek, S. Roberts, T.T. Topping, Y. Robele, D.E. Koditschek, D.J. Jerolmack, Determination of erosion thresholds and aeolian dune stabilization mechanisms via robotic shear strength measurements, American Geophysical Union (AGU) Fall Meeting, 2017 2017AGUFMEP51C1663Q.
- [51] A. Singh, V. Magnanimo, K. Saitoh, S. Luding, Effect of cohesion on shear banding in quasistatic granular materials, *Phys. Rev. E* 90 (2) (2014) 022202.